Journal of The Electrochemical Society

Shape Dependence on the Electrochemistry of Uncoated Magnetite Motifs

Journal of The Electrochemical Society, 2022 **169** 080512
1945-7111/2022/169(8)/080512/9/$40.00 © 2022 The Electrochemical Society ("ECS"). Published on behalf of ECS by IOP Publishing Limited

Shape Dependence on the Electrochemistry of Uncoated Magnetite Motifs

Kenna L. Salvatore,[1,=] Mallory N. Vila,[1,2,=,*] Scott C. McGuire,[1] Nathaniel Hurley,[1] Citlalli Rojas Huerta,[4] Esther S. Takeuchi,[1,2,3,5] Kenneth J. Takeuchi,[1,2,3,5,*] Amy C. Marschilok,[1,2,3,5,*] and Stanislaus S. Wong[1,z]

[1]*Department of Chemistry, State University of New York at Stony Brook, Stony Brook, New York 11794-3400, United States of America*
[2]*Institute of Electrochemically Stored Energy, State University of New York at Stony Brook, Stony Brook, New York 11794-3400, United States of America*
[3]*Department of Materials Science and Chemical Engineering, State University of New York at Stony Brook, Stony Brook, New York 11794-3400, United States of America*
[4]*Department of Chemistry, Trinity College, Hartford, Connecticut 06106, United States of America*
[5]*Interdisciplinary Science Department, Brookhaven National Laboratory, Upton, New York 11973-5000, United States of America*

Using a variety of synthetic protocols including hydrothermal and microwave-assisted methods, the morphology of as-prepared magnetite has been reliably altered as a means of probing the effect of facet variations upon the resulting electrochemical processes measured. In particular, motifs of magnetite, measuring ~100 to 200 nm in diameter, were variously prepared in the form of cubes, spheres, octahedra, and plates, thereby affording the opportunity to preferentially expose either (111), (220), or (100) planes, depending on the geometry in question. We deliberately prepared these samples, characterized using XRD and SEM, in the absence of a carbonaceous surfactant to enhance their intrinsic electrochemical function. Herein, we present a direct electrochemical comparison of specifically modified shape morphologies possessing 3 different facets and their impact as electrode materials for Li-ion batteries. Our overall data suggest that the shapes exhibiting the largest deliverable capacities at various current densities incorporated the highest surface energy facets, such as exposed (220) planes in this study. The faceted nature of different morphologies highlighted a trend in electrochemistry of (220) > (111) > (100); moreover, the degree of aggregation and polydispersity in prepared samples were found to play key roles as well.
 [DOI: 10.1149/1945-7111/ac8626]

Manuscript submitted June 2, 2022; revised manuscript received July 17, 2022. Published August 16, 2022.

Supplementary material for this article is available online

Magnetite (Fe_3O_4) has been thoroughly explored as a viable anode alternative for lithium-ion battery (LIB) applications, due to factors such as relative non-toxicity, low-cost, and plentiful abundance. Moreover, it possesses a high theoretical capacity of 926 mAh g^{-1} as compared with common commercial anodes, such as graphite, which is limited by its significantly lower theoretical capacity at 372 mAh g^{-1}.[1,2] Nevertheless, problems associated with the widespread application of magnetite within batteries include its poor capacity retention during cycling, due to poor diffusion of Li ions, a relatively high volume expansion, and the presence of iron aggregation, as a result of the conversion reaction during the charging/discharging process, which is described by Eq. 1.[2]

$$Fe_xO_y + 2ye^- + 2yLi^+ \leftrightarrow xFe + yLi_2O \quad [1]$$

In particular, the issue with magnetite-based nanomaterials revolves around overcoming a rapid decrease in capacity during cycling, which leads to a decrease in battery activity, in part as a result of SEI (i.e., solid-electrolyte interphase) formation. The presence of SEI production is deleterious to the performance of not only magnetite but also other metal oxide materials. In effect, SEI, which originates from side reactions, is often generated as early as the first cycle and forms a passivating layer over the active sites of the material, thereby resulting in a decrease in the observed activity of the material. A viable method for overcoming this issue would be to generate homogeneous, uniform populations of monodisperse and distinctive magnetite shapes to expose specific reactive facets with the ultimate goal of probing the effects of shape-driven electrochemical processes. Previously, studies of shape-induced performance have focused on systems, such as but not limited to Fe_2O_3,[3] TiO_2,[4] CuO,[5] and $SnFe_2O_4$[6] for a variety of applications, including photocatalysis, 4-nitrophenol reduction, and opto-electronic devices.

With respect to magnetite for incorporation within battery-related applications, we note that doping with magnesium apparently impacted the observed morphology and resulting electrochemical performance. Specifically, by changing the amount of Mg doped within the magnetite sample, the morphology was found to evolve from cubes, cuboctahedra, and ultimately octahedra with correspondingly different exposed planes ranging from (111) to (100). The resulting octahedra incorporating the highest amount of Mg doping yielded an increased cycling performance as compared with that of the other morphologies produced; these motifs maintained a discharge capacity (after 500 cycles) of 803.5 mA h g^{-1} at 1 A g^{-1} coupled with a rate capability of 661.5 mA h g^{-1} when cycled at 4 A g^{-1}.[7] Furthermore, another study explored the effects of exposing (111) and (100) facets of magnetite polyhedra for LIB applications, implying the significance of expanding the number of unique and potentially more reactive facets as a means of improving their activity.[8] Therefore, given this literature precedence, within this work, we intend to probe the roles of (i) the nature of exposed facets and (ii) the associated morphology with respect to measured electrochemical performance within the context of acquiring insights into structure-property correlations relevant for battery applications.

The idea of preferentially generating morphology-driven facets for enhancing electrochemical performance is well established. In fact, morphology-induced facet formation impacted the performance of batteries in oxide materials, such as but not limited to Co_3O_4,[9] Cu_2O,[10] $LiMn_{1.5}Ni_{0.5}O_4$,[11] TiO_2,[12] Fe_2O_3,[13] and finally Fe_3O_4.[14] As an example, changes in dimensionality within titania-based systems, i.e. zero-dimensional (0D), one-dimensional (1D), two-dimensional (2D), versus three-dimensional (3D), led to noticeable improvements in the measured electrochemical performance, wherein 3D TiO_2 urchins were found to yield higher activity as compared with their

[=]Equal Contribution.
[*]Electrochemical Society Member.
[z]E-mail: stanislaus.wong@stonybrook.edu

0D nanoparticles and 1D nanowire counterparts, likely due to an increased Li ion diffusion. Such rational control over morphology gave rise to not only a high capacity retention of ~90% but also stable rate capabilities of 214, 167, 120, 99, and 52 mAh g^{-1} under discharge rates of 0.1, 1, 10, 20, and 50 C respectively.[12] Furthermore, polyhedra of Cu_2O, as manifested in the form of cubes, octahedra, and two types of truncated octahedra, were investigated for their electrochemical activity, in part because they exposed various types of facets, namely (100) and (111) planes. In this latter series, the measured activity gave rise to a distinctive trend with cubes > octahedra > truncated (100) and (110) octahedra, implying a corresponding pattern in facet activity of (100) > (111) > (110).[10] Overall, this collective literature precedence emphasized the significance of correlating electrochemical activity with morphology-induced facet formation within a series of otherwise identical 0D particles.

The other key point worth highlighting is that many of the synthetic processes used to produce homogeneous samples often involve the mediation of organic ligand species, such as oleic acid, which are crucial to the formation of these well-defined controlled aggregate clusters. However, one significant shortcoming of many of these ligands is that they are non-conductive, impede electronic transport, and can hinder the attainment of optimal electrochemical performance.[15] Therefore, not surprisingly, recent studies have sought to remove and substitute these organic ligands after the synthesis process by using treatments involving hydrazine,[16] chemical functionalization,[15] and/or the formation of a uniform outer carbon layer upon annealing.[17] As such, in the studies reported herein, in the preparation of our samples, we have consciously sought to minimize the presence of such extraneous and "interfering" species.

In effect, comparatively few studies have explored the idea of tuning facet formation, via shape and morphology, of monodisperse magnetite nanoparticles in the context of enhancing battery performance.[8,14,17,18] Notably, it has been shown that Fe_3O_4 octahedra yielded a higher cycling performance as compared with that of cubes and cuboctahedra, thereby highlighting the importance of the exposed surface in dictating the observed electrochemical properties of as-prepared magnetite nanomaterials.[8] In essence, our overall strategy has been to fabricate consistent, standardized series of monodisperse motifs of colloidal magnetite nanocrystals[17–28] by carefully tuning size, shape, and chemical composition through meticulous parameter selection.[29]

In so doing, we have concentrated on exploring the electrochemical activity of well-defined 0D and 2D structures of magnetite. Specifically, we have synthesized a series of morphological analogues, such as cubes, spheres, plates, rhombohedra, and octahedra, using variations of solution-based hydrothermal protocols to selectively generate each targeted shape. These reactions have been run under basic conditions with the occasional use of surfactants,[30] without potentially damaging the overall magnetite structure through either (i) high-temperature annealing or (ii) physical deformation of the constituent monodisperse magnetite particles.

This study focuses on the facile synthesis of nanoscale morphology-driven shape control of magnetite analogues with the expectation of correlating facet exposure with the resulting electrochemical performance. In essence, by the optimized creation of controlled morphologies of monodisperse magnetite nanoparticles, we can achieve tangible benefits by enhancing not only the available active surface area and well-defined pathways for electron diffusion to improve upon electron transfer but also the inherent monodispersity of our nanoscale samples, which will reduce SEI formation and maintain overall capacity, all of which should improve upon anode performance as compared with the commercial standard. As a result, this report will consider various morphological manifestations of magnetite, including but not limited to spheres, cubes, octahedra, rhombohedra, and plates, using well known and reasonable synthetic protocols, so as to correlate geometry with the observed electrochemical performance. As such, our overall goal is to not only improve upon overall conductivity but also achieve high-capacity retention by probing facet-driven electrochemical activity through the controlled synthesis of magnetite.

Experimental Section

Materials.—Materials were used, as received. Specifically, $FeCl_3$ (ACS reagent, 97%), ferrous sulfate (98%, Thermo Scientific), potassium hydroxide (ACS Certified reagent), sodium hydroxide (98.5%, Acros Organics), ethylene glycol (Fisher), polyethylene glycol (PEG, MW = 4000) (Alfa Aesar), sodium acetate trihydrate (>99%, Sigma Aldrich), and DI water were all utilized, as procured, without any additional purification protocols involved.

Synthesis of various morphologies of Fe_3O_4.—To generate the relevant materials, both hydrothermal-based and microwave-assisted procedures in general were chosen, due to their relative ease of use and their capability of achieving high reaction yields, to produce sufficient quantities of samples characterized by high phase purity, high crystallinity, and narrow particle size distributions for subsequent electrochemical testing. By contrast, other reaction methods, such as either hot injection or reflux protocols, are limited by their incorporation of carbon-based surfactants, which can interfere with the measured electrochemical performance.

Octahedra.—Within octahedral-based motifs, the (111) facet of magnetite is exposed. Previous literature methods have achieved this synthetic objective by using lower amounts of base, i.e. a decrease in pH, to create this desired morphology.[31] At a lower pH value, lower amounts of adsorbed OH^- ions tend to adsorb onto the growing Fe–O planes, thereby favoring the growth of quasi-spherical, effectively isotropic Fe_3O_4 nanoparticles. By contrast, increased levels of adsorbed OH^- ions can enable the formation of less accessible anisotropic (110) and (111) facets and their higher associated E_{ads} energies, as suggested by DFT calculations.[31]

The following method utilizes sodium hydroxide as the base source in the presence of a small amount of surfactant, such as PEG. Specifically, based on a previous publication,[31] 1 g of NaOH was dissolved in 40 ml EG under heating. Then 1 ml PEG was added. Finally, 1.35 g of $FeCl_3$ was introduced to the heated solution, which was subsequently stirred for 30 min. After this solution was placed into a Teflon steel autoclave, it was heated in an oven for 24 h at 200 °C.

Spheres.—To generate the corresponding spheres, the addition of sodium acetate (NaAc) as opposed to a change in pH was the determinant synthetic factor. The presence of NaAc tends to decrease particle aggregation by introducing repulsive electrostatic interactions. Moreover, NaAc also assists in the reduction of $FeCl_3$ to Fe_3O_4.[32] In particular,[33] 50 mmol NaAc was dissolved in 40 ml EG, after which 1.35 g $FeCl_3$ was added. The solution was then stirred for 30 min followed by heating in a stainless-steel autoclave at 200 °C for 10 h. In prior literature, similar types of reactions have been shown to yield spheres, characterized by a (220) facet.[34]

Cubes.—Analogous to the procedure used to fabricate octahedra in which pH variations were crucial to achieving the resulting morphology, in this example, we used potassium hydroxide (KOH) as opposed to sodium hydroxide. Furthermore, the identity of the iron salt precursor was modified as well. In so doing, these cumulative changes enabled us to favor the formation of (100)-faceted cubes as opposed to (111)-faceted octahedra. With respect to the protocol used,[35] a 0.5 M KOH solution was produced using 5 ml EG. Subsequently, 0.28 g $FeSO_4$ was added to the solution followed by stirring for 30 min. Ultimately, the solution was heated in a stainless-steel autoclave at 200 °C for 24 h.

Plates.—Based on an in-house modification of a prior protocol,[36] hexagonal plates of Fe_3O_4 were generated using a facile microwave-

assisted procedure. Microwave-enabled methods are known for their facile ease of use, rapid reaction times (usually < 30 min), and ability to generate large yields of high-quality, crystalline products, by analogy with samples prepared using hydrothermal reactions. In this case, $FeSO_4$ (0.2 g) was introduced into 10 ml H_2O. Subsequently, 2 ml of ethylene glycol was added. Finally, a 2 ml NaOH solution (0.2 g) was put in, so as to generate a green solution. As opposed to the original published reaction, wherein the solution was heated to reflux under microwave irradiation for a designated amount of time, in our case, we completely avoided these higher-temperature reflux conditions. Instead, the sample solution was sufficiently stirred, placed into a microwave reaction chamber (CEM Discover), and ultimately irradiated under a "closed-vessel" reaction environment at 100 °C for 10 min.

Characterization methods.— *X-ray diffraction (XRD).*—Powder X-ray diffraction has been utilized to analyze the crystallographic information and to confirm the chemical composition of as-prepared samples. To prepare the XRD sample for analysis, the product was dispersed in acetone via sonication, and then deposited onto a zero-background holder (MTI Corporation, Zero diffraction plate for XRD, B-doped, p-type Si, 23.6 mm in diameter by 2 mm in thickness). The Rigaku Miniflex diffractometer was used to obtain sample powder XRD data, taken in the Bragg configuration with Cu Kα radiation ($\lambda = 1.5418$ Å), operating in the 2θ range of 10°–80° utilizing a scan rate of 10 degrees per minutes.

Electron microscopy.—We employed scanning electron microscopy (SEM) to acquire key information about sample morphology and sample size. Specifically, SEM data were collected using a Hitachi 4800 S instrument under 10 kV voltage conditions. To prepare our various SEM samples for characterization, powders of as-generated Fe_3O_4 nanomaterials were dispersed in ethanol prior to drop-casting aliquots onto a silicon wafer. Complementary high resolution transmission electron microscopy (HRTEM) images data were acquired using a JEOL JEM-2100F microscope, operating with an acceleration voltage of 200 kV. Relevant samples were prepared through their dispersal in ethanol, followed by drop-casting onto a lacey carbon-coated Cu grid.

Thermogravimetric analysis (TGA).—TGA was run using a TA instruments Q500. In particular, 20–30 mg of Fe_3O_4 powders were dried, loaded into a clean 50 μl Pt pan, and ultimately heated to 600°C at a rate of 10 deg/min. The temperature was chosen to ensure the complete degradation of any organic components on the surfaces of the nanoparticles. Compressed air and anhydrous nitrogen were used as the carrier gasses with a flow rate of 40 ml min^{-1} and 120 ml min^{-1} respectively, throughout the as-obtained measurements.

Fourier transform infrared (FT-IR) spectroscopy FT-IR measurements were acquired on a Thermo Scientific Nicolet iS10 instrument. Powders of the various iron oxide samples were dried in order to ensure that no background signal emanated from the solvents. Samples were placed onto a diamond anvil and scanned for a total of 16 times.

Electrochemistry.—The electrochemistry of the samples was assessed using cyclic voltammetry, galvanostatic cycling over a series of rates, and galvanostatic cycling at a fixed rate. Commercial Fe_3O_4 (Sigma-Aldrich) was used by means of comparison as a control sample; the associated characterization data on the composition, size, and morphology of these materials are provided in Figs. S1 and S2. Electrodes were prepared using slurries of the Fe_3O_4 samples with carbon black and polyvinylidene fluoride (PVDF) in a 70: 20: 10 weight ratio, which were cast onto a copper foil. The mass range of the active material was 1.44 ± 0.2 mg cm^{-2} for all of the electrode samples. Coin type cells were assembled using a Li metal foil with 1 M $LiPF_6$ in the presence of a 3:7 (vol.: vol.) ethylene carbonate and dimethyl carbonate electrolytic mixture under an inert atmosphere. Cyclic voltammetry data were acquired using a voltage range of 0.05 to 2.8 V for 5 cycles at 0.2 mV/s. The cells were tested using rates of 200, 400, 800, 1600, and 200 mA g^{-1}, respectively, for 10 cycles each from 0.05 to 2.8 V. Complementary galvanostatic cycling data were collected for 100 cycles at 200 mA g^{-1} with the same voltage range. Electrochemical impedance spectroscopy data were collected using a Biologic VSP potentiostat. All of the electrochemical testing was conducted at 30 °C.

Results and Discussion

Characterization of magnetite nanoparticles.—To characterize the relevant materials, XRD was initially conducted as a means of probing the composition and crystallinity of as-prepared materials. It is worth noting that we were able to isolate the pure spinel crystal pattern for all 4 materials generated, namely octahedra (red), spheres (orange), cubes (yellow), and plates (green), respectively (Fig. 1). In effect, the corresponding diffraction patterns could be ascribed to the standard pattern, expected for magnetite (JCPDS # 19–0629, black).

Complementary structural characterization of our variously prepared magnetite samples was accomplished using SEM, and the associated morphological data are presented in Fig. 2. As-generated octahedra averaged 116 ± 14 nm in diameter (Figs. 2A and 2B; Table I). Fe_3O_4 spheres evinced dimensions on the order of 261 ± 55 nm (Figs. 2C and 2D; Table I). Cubes exhibited an average size of 170 ± 22 nm (Figs. 2E and 2F; Table I), whereas our as-produced plates gave rise to widths of 179.8 ± 67.7 nm, coupled with measured thicknesses on the order of 21.9 ± 5.2 nm (Figs. 2G and 2H; Table I).

It is worth reinforcing that the objective of generating these various motifs was to expose selective facets and to examine the electrochemical ramifications of doing so. As previously implied above, the facets of these aforementioned nanomaterials can be assigned, as follows: plates evince a (111) facet on its main hexagonal face coupled with an orthogonal (111) plane on its shorter dimension (Fig. 3A). Octahedra exhibit a (111) plane on

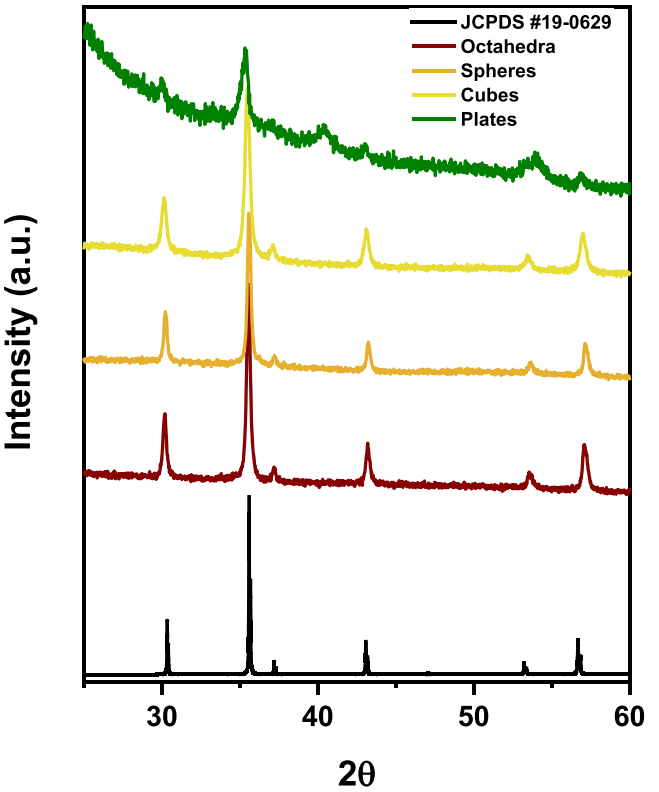

Figure 1. Measured XRD patterns of octahedra (red), spheres (orange), cubes (yellow), and plates (green), coupled with the database standard for magnetite #19–0629.

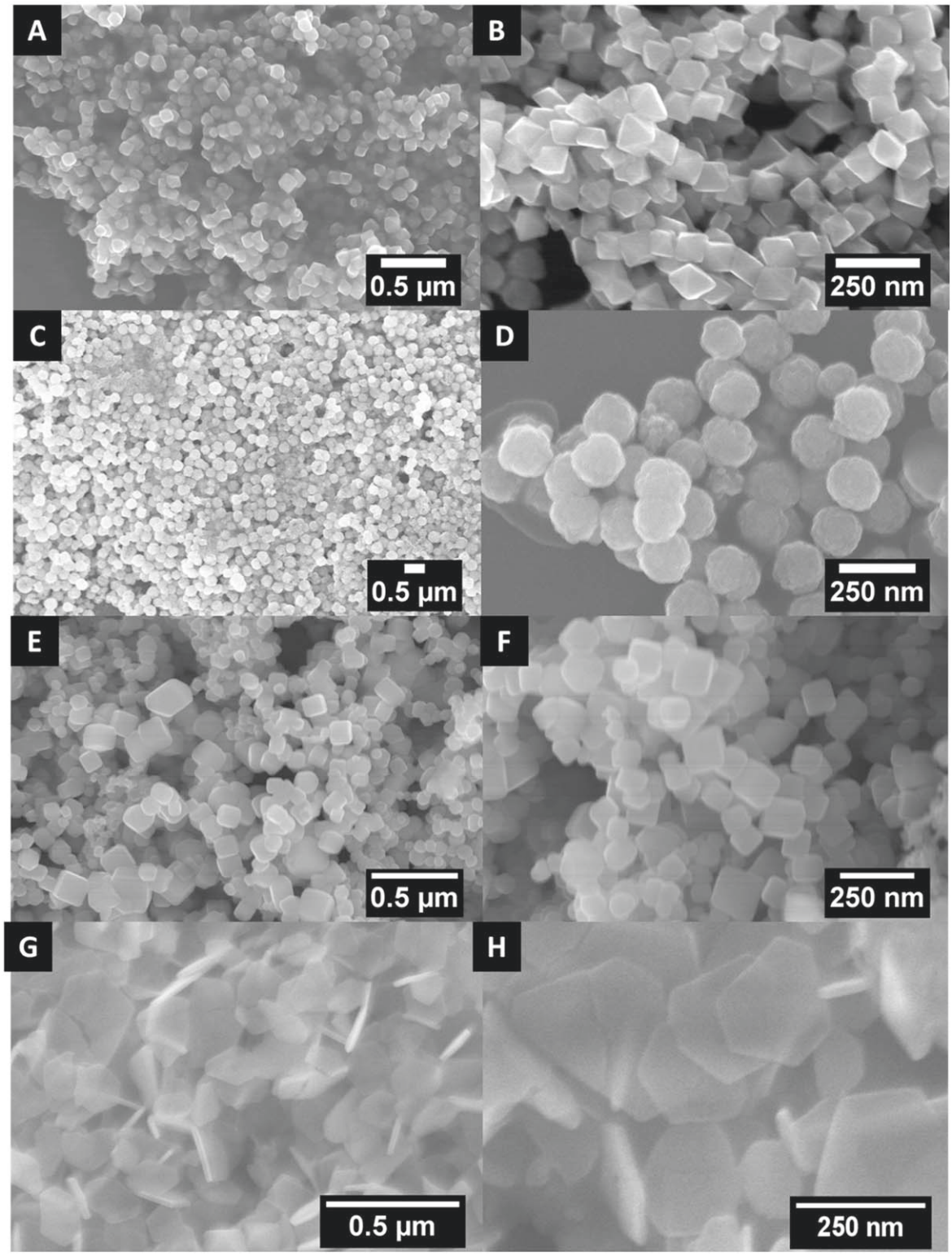

Figure 2. SEM images of as-prepared samples of (A/B) octahedra, (C/D) spheres, (E/F) cubes, and (G/H) plates of magnetite (Fe_3O_4).

all 8 of its variously exposed faces (Fig. 3B). Cubes give rise to a (100) plane on its 6 identical faces (Fig. 3C). Finally, spheres are generally isotropic, but past literature has indicated the presence of a (220) planar facet in analogous systems (Fig. 3D).[34] These assertions were further explored and corroborated using HRTEM and *d*-spacing analysis of the various samples (Fig. 4).

With respect to octahedra, the HRTEM image confirmed the distinctive morphology observed in the SEM image (Fig. 4A); we detected an exposed (111) facet by *d*-spacing analysis with a measured d_{111} plane spacing of 0.5 ± 0.02 nm (Fig. 4B). Spheres also exhibited the expected morphology in its HRTEM image (Fig. 4C); the corresponding *d*-spacing analysis revealed the presence of a (220) facet, associated with a d_{220} plane measurement of 0.30 ± 0.03 nm (Fig. 4D). Regarding the sample of cubes, the anticipated morphology was noted in its HRTEM image (Fig. 4E) with its corresponding (100) facet, characterized by a d_{100} plane

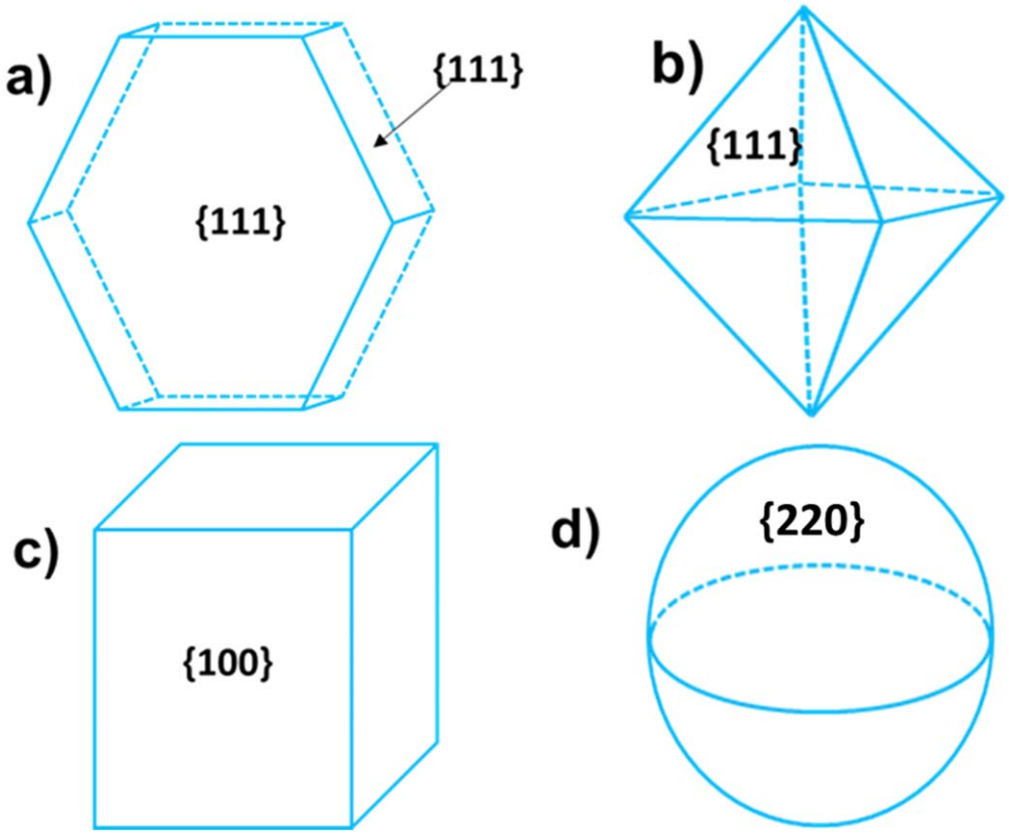

Figure 3. Schematic of various exposed planar facets of Fe_3O_4 encompassing (A) plates, (B) octahedra, (C) cubes, and (D) spheres.

Table I. Sizes and Shapes of Variously-Prepared Fe_3O_4 materials.

Morphology	Measured Size
Octahedra	116 ± 14 nm
Spheres	261 ± 55 nm
Cubes	170 ± 22 nm
Plates	179.8 ± 67.7 nm in width; 21.9 ± 5.2 nm in thickness

measurement of 0.84 ± 0.01 nm (Fig. 4F). Finally, the plates displayed the projected morphology, when analyzed by HRTEM (Fig. 4G); we identified the presence of (111) facets via *d*-spacing analysis, wherein the lattice spacing was found to be 0.49 ± 0.02 nm (Fig. 4H). All of these measurements are consistent with previously published data for various as-synthesized magnetite motifs, thereby not only validating the effectiveness of our syntheses but also enabling an effective study of shape-dependent electrochemical behavior.[37]

SAED measurements also confirmed the chemical composition and structure in a manner consistent with the prior XRD and HRTEM data (Fig. S3).

Furthermore, FT-IR and TGA measurements were acquired to ascertain if any residual carbon from the synthesis processes remained on the particle surfaces (Fig. S4). Regarding the IR of the commercial plates, cubes, octahedra, and spheres (Figs S4B, D, F, H, and J respectively), the resulting spectra showed the presence of a weak peak at ∼3200 cm^{-1} attributed to –OH stretching coupled with a peak at ∼600 cm^{-1}, indicative of Fe–O. Additionally, there was evidence for C–O stretching vibrations at ∼1030 cm^{-1} in all of the samples analyzed.[38,39] Moreover, several samples including cubes, plates, and spheres also gave rise to the presence of a C-H stretching mode at 2918 cm^{-1}. With respect to the TGA analysis (Figs. S4, A, C, E, G, I respectively), all materials exhibited the same pattern of expected mass loss, wherein the initial stage of mass loss ending at 120 °C could be attributed to not only the removal of surface bound water but also the oxidation of Fe_3O_4 to Fe_2O_3.[40] We also noted a second distinctive region in which mass was slowly lost up to 600 °C. This additional stage could be ascribed to the removal and burning off of organic components. These processes are summarized in Table S1. We found similar behavior in all of the samples and not simply ones that incorporated surfactant. As such, we can assign these cumulative TGA and IR findings either to the presence of residual organic solvent or the exposure of these samples to air, since these observations were present in all samples, regardless of whether surfactant molecules were expected or not.

Electrochemical characterization.—Representative cyclic voltammograms of the commercial material and of as-synthesized Fe_3O_4 samples are summarized in Fig. 5. The commercial sample showed a cathodic peak at 0.62 V, attributed to the reduction of $Fe^{3+} \rightarrow Fe^{2+}$ and finally $Fe^{2+} \rightarrow Fe^0$.[41–43] Upon oxidation, a peak situated at∼1.60 V with a shoulder at ∼1.90 V appeared and could be ascribed to the conversion of Fe^0 to Fe^{2+}.[44] The anodic and cathodic peaks (∼0.8 V and ∼2.0 V, respectively) during cycles 2–5 represent the redox processes of the conversion from FeO to Fe^0. The as-synthesized materials (Figs. 5B–5E) showed similar potentials, corresponding to the values at which the relevant redox mechanisms would be expected to occur. Notably, the sample characterized by the plate morphology evinced a small peak at ∼1.55 V with another peak at ∼0.75 V at cycle 1. Significantly, the reduction of Fe^{3+} to Fe^{2+} will take place for all of the material samples, as the reduction process itself progresses.

However, it has been determined by both experiment and DFT that nano-crystalline magnetite can incorporate surfaces that contain oxidized iron oxide phases, specifically maghemite, γ-Fe_2O_3.[45] It is the presence of this oxidized iron phase that accounts for the initial

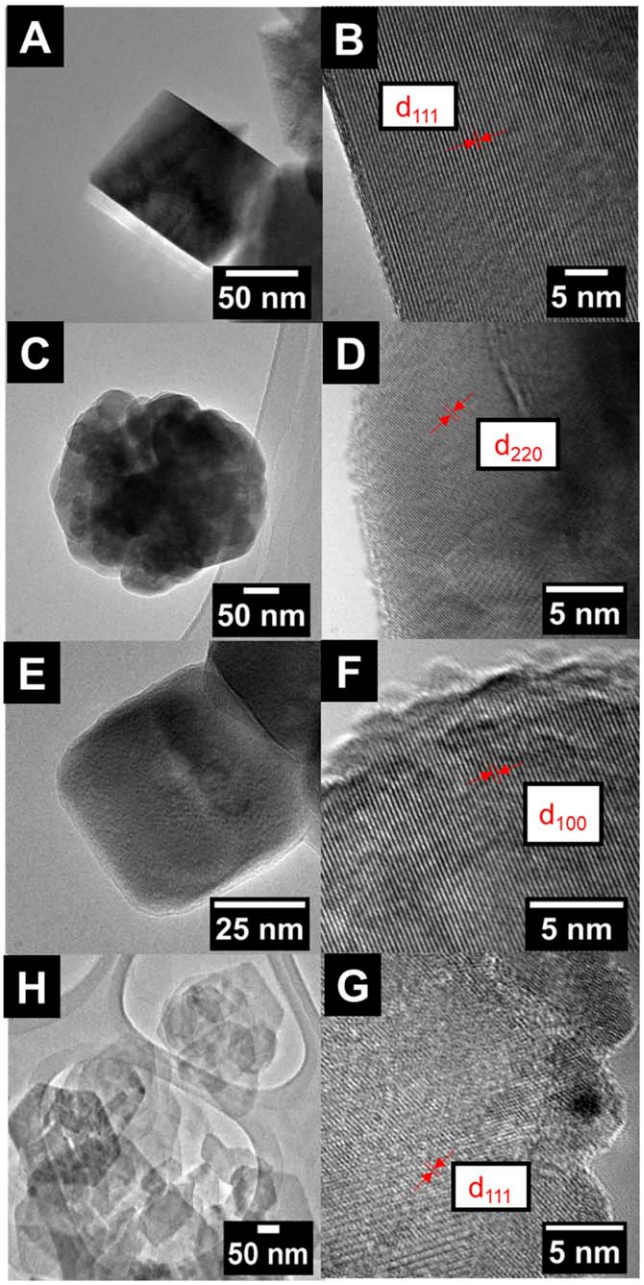

Figure 4. HRTEM and corresponding *d*-spacing measurements for as-prepared samples of (A and B) octahedra, (C and D) spheres, (E and F) cubes, and (H and G) plates.

voltage observed, according to DFT calculations. Thus, it is likely that the plate morphology, possessing a high surface-to-internal bulk ratio due to its intrinsic geometry, contains a sufficient amount of maghemite to demonstrate this higher voltage reduction, as noted in the initial voltammograms.

A typical Fe_3O_4 voltammogram would exhibit a peak at ~1.55 V, indicative of Fe^{3+} to Fe^{2+} reduction.[41–43] Throughout cycles 2–5, there is a decrease in the peak currents with a corresponding increase in the anodic peak voltages. The plate morphology generated a different profile, wherein the initial reduction of Fe^{3+} takes place at higher potentials (i.e., 1.55 V and 0.75 V for plates versus 0.62 V for the commercial material), as discussed above.

Rate capability measurements of the material samples were performed at 200, 400, 800, 1600, and 200 mA g^{-1} current densities for 50 cycles (Fig. 6A). The respective voltage profiles for the commercial standard (Fig. 6B) and for the as-synthesized samples (Figs. 6C–6F) at the first cycle of each current density change are shown. During the first lithiation, the commercial standard delivered 1023 mAh g^{-1}, while at end of the 10 cycles at 200 mA g^{-1}, the supplied capacity was half of the original. The first discharge profile displayed a voltage plateau starting at ~125 mAh g^{-1} (0.82 V), wherein 46% of the measured capacity occurred within this plateau. The first charge exhibited a sloped profile with a plateau covering a range from 1.5 to 2.0 V. As the current was increased to 400, 800, and 1600, and later decreased to 200 mA g^{-1}, the commercial material achieved 475, 360, 259, and 213 mAh g^{-1} on cycles 11, 21, 31, and 41, respectively, and by the end of cycle 50, it yielded 630 mAh g^{-1}.

The as-synthesized spherical sample provided for higher capacities at each rate and was able to maintain 62% of its capacity at the end of 50 cycles from cycle 2 (790 mAh g^{-1} at cycle 2; 491 mAh g^{-1} at cycle 50). At 400, 800, 1600, and 200 mA g^{-1}, the spheres reached 638, 514, 390, and 344 mAh g^{-1} at cycle 11, 21, 31, and 41, respectively. The octahedra initially showed higher capacities than the commercial standard, but were similar to the plates and cubes at higher current densities, retaining 40% capacity from cycle 2 (726 mAh g^{-1} at cycle 2; 288 mAh g^{-1} at cycle 50). The plates and cubes delivered 516 mAh g^{-1} and 431 mAh g^{-1}, respectively, upon the second cycle. The cubes evinced slightly higher lithiation capacities than that of the plates, leading to 43% and 55% capacity retention, respectively, as compared with the starting values measured at cycle 2 (431 mAh g^{-1} for cubes; 516 mAh g^{-1} for plates).

Electrochemical impedance spectroscopy was performed for the analysis of the kinetic behavior of the samples. Cells containing each of the as-synthesized Fe_3O_4 samples prior to galvanostatic testing were constructed and tested (Fig. 7). The results show that the slope of the diffusional part of the Nyquist type plot varies, according to the shape of the Fe_3O_4 material type. Notably, the rank ordering in terms of diffusion is spheres > octahedra > cubes > plates. This rank ordering is consistent with the observed delivered capacity. We note that the electrode loading was deliberately low so as to emphasize the impact of the material itself rather than inclusion of factors related to diffusion at the electrode level. Significantly, there is a prior report on the impact of particle shape on the electrochemical impedance response in which spherical particles were projected to give rise to a faster diffusion response than either cylindrical particles or a planar electrode.[46] The results here are consistent with that prior theoretical study. It should also be mentioned that the narrow particle size distribution of the as-synthesized materials is consistent with the prior theoretical treatment, because a wide distribution of particle sizes can otherwise impact the observations in unexpected ways.

Galvanostatic cycling data were collected for 100 cycles at 200 mA g^{-1} (Fig. 8). The commercial material delivered 954 mAh g^{-1} upon lithiation but decreased to 595 mAh g^{-1} during the second discharge. After 100 cycles, the capacity was 301 mAh g^{-1} with an overall retention of 51% from cycle 2. Notably, the spheres maintained 68% capacity from cycle 2 (894 mAh g^{-1}) in agreement with the rate capability testing data; by the end of the extended cycling process, it yielded 609 mAh g^{-1}. The octahedra exhibited a broad decrease in capacity from cycle ~17–45 with a value of 486 mAh g^{-1} measured at the end of 100 cycles, or a 61% capacity retention from cycle 2. As shown in the rate capability testing results, the plates and cubes demonstrated similar cycling behavior with an increase in the cubes' capacity around cycle 55 for a 78% capacity retention. The plates do not experience this same increase, but rather stabilized at ~230 mAh g^{-1} from cycles 30–100.

Inverse spinel oxide Fe_3O_4 materials have been systematically synthesized to change the morphology of the host material. For an FCC crystal, the surface energies on each plane increase following this trend: (111) < (100) < (110) < (220), wherein as-synthesized nanoparticles will favorably grow on the (111) facet. If the nucleation growth speed is faster on the (111) facet than on (100), the nanoparticles will cover the (111) facet, thereby leading to the

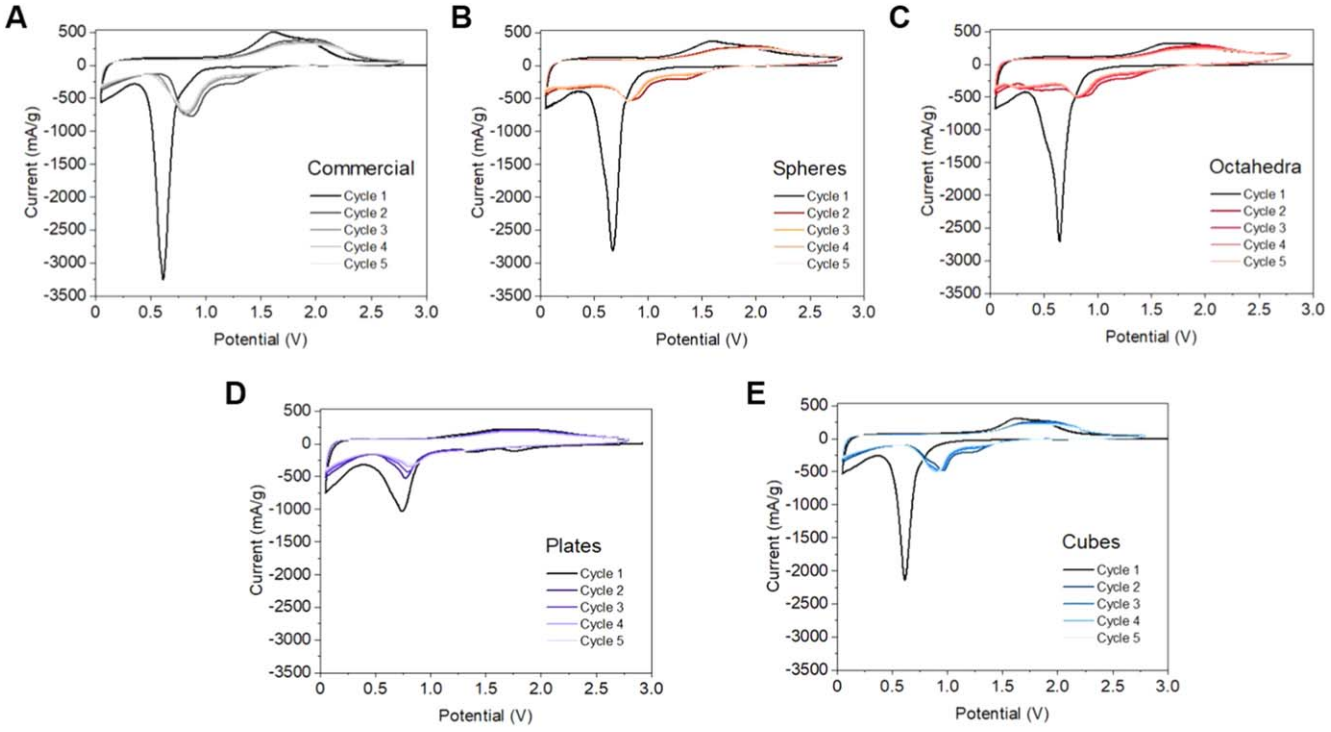

Figure 5. Cyclic voltammograms from 0.05–2.8 V at 0.2 mV s^{-1} of (A) the commercial material and the as-synthesized Fe_3O_4 motifs, in the shape of (B) spheres, (C) octahedra, (D) plates, and (E) cubes.

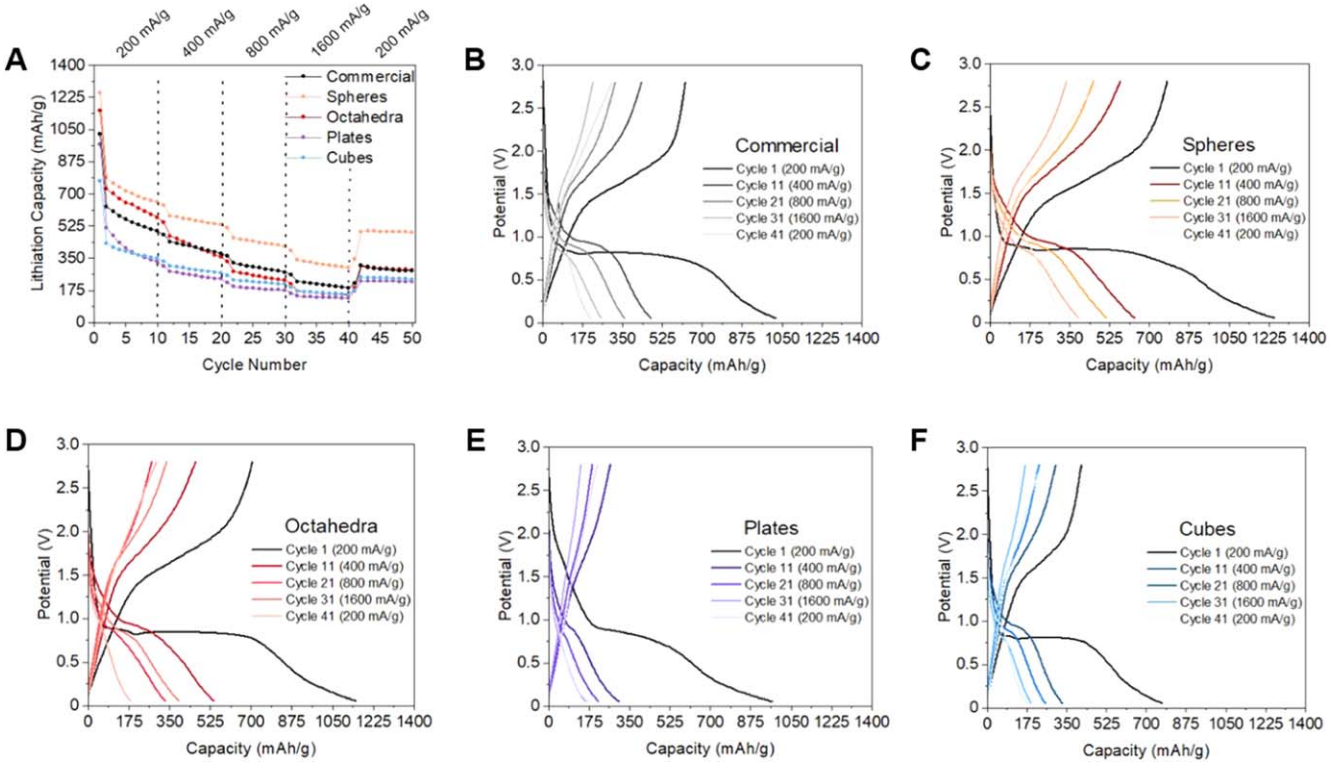

Figure 6. Rate capability of all the commercial and synthesized materials overlaid on each other, as presented in (A). The respective voltage profiles from rate capability testing for (B) the commercial material, (C) spheres, (D) octahedra, (E) plates, and (F) cubes are also shown.

presence of exposed (100) facets in which the isolated structure is determined to contain solely (100) facets.[47] If the opposite occurs, wherein (100) experiences faster nucleation growth than (111), then the synthetic outcome will be an octahedral structure. Plates are comprised of (111) facets with the sides bounded by (100) facets.[48] Although a matter of debate, spheres can either contain solely (220) facets[34] or incorporate (311) planes, as well.[49]

The testing of some magnetite electrodes containing various facets revealed differences in capacity retention, which could be attributed to their crystallographic structures.[8,50–52] A direct

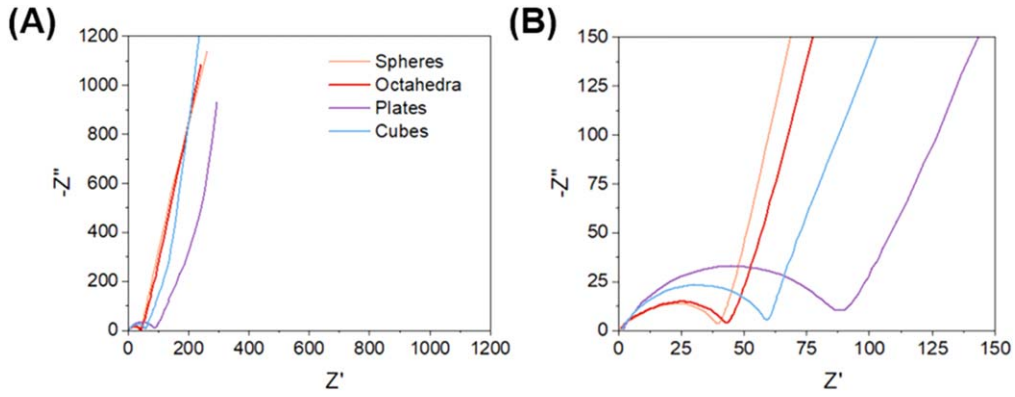

Figure 7. (A) Nyquist plot, with a zoomed-in version of the plot, presented in (B), for all cells using the different, as-synthesized Fe_3O_4 morphologies.

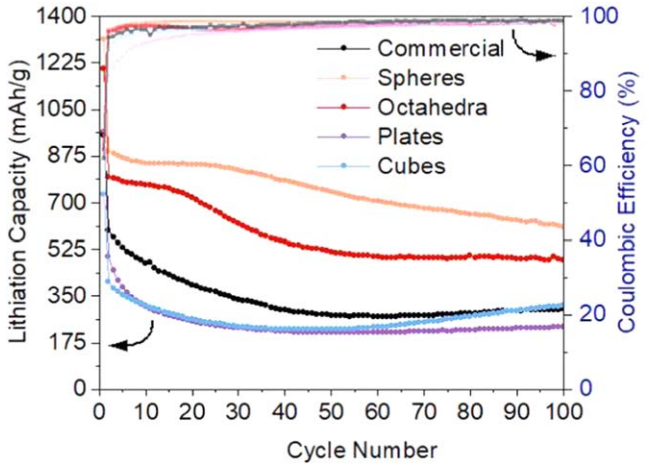

Figure 8. Galvanostatic cycling data of all of the as-synthesized materials in addition to the commercial baseline.

comparison between octahedral and cubic structures revealed an increase in the capacity retention of a (111) facet as compared with that of a (100) facet, in which the (111) facet delivered 883 mAh g^{-1} after 200 cycles versus <500 mAh g^{-1} for the analogous cubic structure, the latter of which is presumed to contain exposed (100) planes. It was also noted that the lower activity of the (100) facet could be ascribed to decreased Fe^{3+} in the host structure with a potentially lower electronic conduction required for efficient Fe^{3+} and Li^+ interaction.[8] Through SEM images, the plates synthesized in this study were characterized by a significant level of aggregation, which may account for the decreased electrochemical activity. It has been previously shown that aggregation leads to a lower delivered capacity, due to transport limitations; however, particle agglomeration can also give rise to an increased capacity retention, due to more limited SEI formation (Fig. 8, light purple color).[42]

Another study reported on a comparison between a prismatic structure of Fe_3O_4/γ-Fe_2O_3 in the presence and absence of a surface reactant and reducing agent, respectively; these specific architectures incorporated either solely (220) planes or one with (220) and (111) planes, within a Na_2SO_3 cyclic voltammetry experiment.[51] The sample containing exposed (220) and (111) planes was electrochemically dominated by the presence of the (111) plane due to its higher surface area (2x) as compared with that of the (220) plane alone. The experiment demonstrated the enhanced nature of the Fe^{3+}/Fe^{2+} redox couple for the sample solely containing the (220) plane, thereby suggesting that greater numbers of electrochemically active species that could participate in lithiation are likely present in higher index planes. As a result, of the various synthesized materials that were of interest and tested in this paper, the spherical morphology, possessing an exposed plane correlating with the highest surface energy, should be the most stable and deliver the highest capacities throughout the extended cycling process. As demonstrated throughout the testing shown, the as-synthesized spheres indeed delivered ~600 mAh g^{-1} after 100 cycles and yielded superior cycling at higher current densities. By contrast, the commercial sample gave rise to less capacity, likely due to its larger size; however, it still outperformed the plates and cubes, containing the (100) facet.

Conclusions

Magnetite nanostructures, including octahedra, plates, cubes, and spheres, were analyzed for their electrochemical performance as a function of their corresponding exposed planar facets, namely the (111), (220), and (100) facets of the spinel phase of Fe_3O_4. It is worth highlighting that we deliberately chose synthetic protocols that avoided the use of any organic surfactants and additives that might have interfered with the expected electrochemical metrics for this system. To more precisely analyze the role and effect of shape, other variables including size and composition were kept constant. Significantly, in these experiments, based on XRD and SEM data, we were able to evaluate a series of apparently pure and homogeneous magnetite motifs, measuring ~100 to 200 nm in dimension.

In summary, the shape morphology of the Fe_3O_4 host material impacted the Coulombic efficiency, the capacity retention, and nature of the Li^+ interactions. The shape exhibiting the highest deliverable capacities at various current densities incorporated exposed (220) planes. The faceted nature of the different morphologies analyzed highlighted a trend in electrochemical performance, wherein (220) > (111) > (100); however, the facets dominating each shape were not the only factor contributing to enhanced lithiation abilities. Instead, the degree of sample aggregation and polydispersity were likely to be important considerations as well. Overall, this paper presents a direct comparison of specifically modified shape morphologies possessing 3 different facets and their impact as electrode materials for Li-ion batteries. The synthetic techniques described in this paper in selectively exposing certain facets can be beneficial for the future testing of additional series of Fe_3O_4–based electrodes.

Acknowledgments

All of the work described in these studies was funded as part of the Center for Mesoscale Transport Properties (m2M), an Energy Frontier Research Center supported by the U.S. Department of Energy, Office of Science, Basic Energy Sciences, under award #DE-SC0012673. Experimental research characterization was carried out in part at the Center for Functional Nanomaterials, Brookhaven National Laboratory, an Office of Science User Facility, which is supported by the U.S. Department of Energy, Office of Basic Energy Sciences, under Contract No. DE-

SC0012704. E.S.T. acknowledges funding from the William and Jane Knapp Chair for Energy and the Environment. C.R.H acknowledges support from the National Science Foundation (CHE-2050541).

ORCID

Mallory N. Vila https://orcid.org/0000-0002-8745-1159
Esther S. Takeuchi https://orcid.org/0000-0001-8518-1047
Kenneth J. Takeuchi https://orcid.org/0000-0002-9345-6503
Amy C. Marschilok https://orcid.org/0000-0001-9174-0474
Stanislaus S. Wong https://orcid.org/0000-0001-7351-0739

References

1. N. Nitta, F. Wu, J. T. Lee, and G. Yushin, *Mater. Today*, **18**, 252 (2015).
2. S. Goriparti, E. Miele, F. De Angelis, E. Di Fabrizio, R. Proietti Zaccaria, and C. Capiglia, *J. Power Sources*, **257**, 421 (2014).
3. T. Wang, S. Zhou, C. Zhang, J. Lian, Y. Liang, and W. Yuan, *New J. Chem.*, **38**, 46 (2014).
4. J. Du, J. Zhang, and D. J. Kang, *CrystEngComm*, **13**, 4270 (2011).
5. S. Konar, H. Kalita, N. Puvvada, S. Tantubay, M. K. Mahto, S. Biswas, and A. Pathak, *J. Catal.*, **336**, 11 (2016).
6. E. Zhang, L. Wang, B. Zhang, Y. Xie, and G. Wang, *J. Sol-Gel Sci. Technol.*, **89**, 355 (2019).
7. C. Ding, Y. Zeng, L. Cao, R. Li, Y. Zhang, and L. Zhao, *RSC Adv.*, **6**, 53331 (2016).
8. C. Ding, X. Jiang, X. Huang, H. Zhang, W. Zhong, Y. Xia, and C. Dai, *Mater. Res. Bull.*, **97**, 142 (2018).
9. R. Gao, J. Zhu, X. Xiao, Z. Hu, J. Liu, and X. Liu, *J. Phys. Chem. C*, **119**, 4516 (2015).
10. K. Chen, S. Song, and D. Xue, *CrystEngComm*, **17**, 2110 (2015).
11. B. Hai, A. K. Shukla, H. Duncan, and G. Chen, *J. Mater. Chem. A*, **1**, 759 (2013).
12. C. S. Lewis, Y. R. Li, L. Wang, J. Li, E. A. Stach, K. J. Takeuchi, A. C. Marschilok, E. S. Takeuchi, and S. S. Wong, *ACS Sustain. Chem. Eng*, **4**, 6299 (2016).
13. H. Liu and G. Wang, *J. Mater. Chem. A*, **2**, 9955 (2014).
14. C. Ding, Y. Zeng, R. Li, Y. Zhang, and L. Zhao, *J. Alloys Compd.*, **676**, 347 (2016).
15. K. Kravchyk, L. Protesescu, M. I. Bodnarchuk, F. Krumeich, M. Yarema, M. Walter, C. Guntlin, and M. V. Kovalenko, *J. Am. Chem. Soc.*, **135**, 4199 (2013).
16. K. V. Kravchyk, L. Piveteau, R. Caputo, M. He, N. P. Stadie, M. I. Bodnarchuk, R. T. Lechner, and M. V. Kovalenko, *ACS Nano*, **12**, 8297 (2018).
17. L. Li, T. Wang, L. Zhang, Z. Su, C. Wang, and R. Wang, *Chem. Eur. J.*, **18**, 11417 (2012).
18. S.-D. Seo, D.-H. Lee, H.-W. Shim, S. Lee, and D.-W. Kim, *J. Am. Ceram. Soc.*, **97**, 1413 (2014).
19. S. H. Lee et al., *Nano Lett.*, **13**, 4249 (2013).
20. Y. Jiao, D. Han, Y. Ding, X. Zhang, G. Guo, J. Hu, D. Yang, and A. Dong, *Nat. Commun.*, **6**, 6420 (2015).
21. R. Wang, C. Xu, M. Du, J. Sun, L. Gao, P. Zhang, H. Yao, and C. Lin, *Small*, **10**, 2260 (2014).
22. J.-S. Xu and Y.-J. Zhu, *ACS Appl. Mater. Interfaces*, **4**, 4752 (2012).
23. G. Guo, L. Ji, X. Shen, B. Wang, H. Li, J. Hu, D. Yang, and A. Dong, *J. Mater. Chem. A*, **4**, 16128 (2016).
24. H. S. Lim, D. Kim, J. K. Hwang, Y. J. Kim, Y. K. Sun, and K. D. Suh, *RSC Adv.*, **5**, 42990 (2015).
25. L. Li, H. Wang, Z. Xie, C. An, G. Jiang, and Y. Wang, *J. Alloys Compd.*, **815**, 152337 (2020).
26. W. Qi, X. Li, H. Li, W. Wu, P. Li, Y. Wu, C. Kuang, S. Zhou, and X. Li, *Nano Res.*, **10**, 2923 (2017).
27. Y. Xu, K. Zhu, P. Liu, J. Wang, K. Yan, J. Liu, J. Zhang, J. Li, and Z. Yao, *CrystEngComm*, **21**, 5050 (2019).
28. S. R. Kumar, J. G. Kim, C. Viswanathan, W. B. Kim, R. K. Selvan, and N. Ponpandian, *Mater. Res. Bull.*, **97**, 272 (2018).
29. M. F. Oszajca, M. I. Bodnarchuk, and M. V. Kovalenko, *Chem. Mater.*, **26**, 5422 (2014).
30. D. Wang, B. Lin, T. Shen, J. Wu, F. Hao, C. Xia, Q. Gong, H. Tang, B. Song, and H. Ai, *Chin. Phys. B*, **25**, 077504 (2016).
31. N. Xu et al., *J. Cryst. Growth*, **547**, 125780 (2020).
32. H. Deng, X. Li, Q. Peng, X. Wang, J. Chen, and Y. Li, *Angew. Chem. Int. Ed.*, **44**, 2782 (2005).
33. S. Liu, F. Lu, R. Xing, and J.-J. Zhu, *Chem. Eur. J.*, **17**, 620 (2011).
34. Y. Li, Z. Wang, Z. Ali, K. Tian, J. Xu, W. Li, and Y. Hou, *Science China Materials*, **62**, 1488 (2019).
35. H. Fatima, D.-W. Lee, H. J. Yun, and K.-S. Kim, *RSC Adv.*, **8**, 22917 (2018).
36. W. Wang and J. Yao, *Chem. Lett.*, **43**, 1554 (2014).
37. C. Liang, S. Huang, W. Zhao, W. Liu, J. Chen, H. Liu, and Y. Tong, *New J. Chem.*, **39**, 2651 (2015).
38. I. M. Lourenço, M. T. Pelegrino, J. C. Pieretti, G. P. Andrade, G. Cerchiaro, and A. B. Seabra, *Journal of Physics: Conference Series* **1323** (2019).
39. N. F. M. Rodrigues, S. Y. Neto, R. C. S. Luz, F. S. Damos, and H. Yamanaka, *Biosensors (Basel)*, **8**, 16 (2018).
40. S. Bandi, V. Hastak, C. L. P. Pavithra, S. Kashyap, D. K. Singh, S. Luqman, D. R. Peshwe, and A. K. Srivastav, *J. Mater. Res.*, **34**, 3389 (2019).
41. C. L. McBean, L. Wang, D. Moronta, A. Scida, L. Li, E. S. Takeuchi, K. J. Takeuchi, A. C. Marschilok, and S. S. Wong, *ACS Appl. Energy Mater.*, **2**, 4801 (2019).
42. D. C. Bock, C. J. Pelliccione, W. Zhang, J. Wang, K. W. Knehr, J. Wang, F. Wang, A. C. West, A. C. Marschilok, and K. J. Takeuchi, *ACS Appl. Mater. Interfaces*, **8**, 11418 (2016).
43. Y. Piao, H. S. Kim, Y.-E. Sung, and T. Hyeon, *Chem. Commun.*, **46**, 118 (2010).
44. D. C. Bock, A. C. Marschilok, K. J. Takeuchi, and E. S. Takeuchi, *Chem. Commun.*, **53**, 13145 (2017).
45. C. N. Lininger, C. A. Cama, K. J. Takeuchi, A. C. Marschilok, E. S. Takeuchi, A. C. West, and M. S. Hybertsen, *Chem. Mater.*, **30**, 7922 (2018).
46. J. Song and M. Z. Bazant, *J. Electrochem. Soc.*, **160**, A15 (2012).
47. C. Yang, J. Wu, and Y. Hou, *Chem. Commun.*, **47**, 5130 (2011).
48. L. Chen, Q. Zhou, Q. Xiong, W. Li, J. Liu, and X. Yang, *Adv. Mater. Sci. Eng.*, **2015**, 763124 (2015).
49. X. Lu, R. Wang, Y. Bai, J. Chen, and J. Sun, *J. Mater. Chem. A*, **3**, 12031 (2015).
50. X.-L. Cheng, J.-S. Jiang, D.-M. Jiang, and Z.-J. Zhao, *The Journal of Physical Chemistry C*, **118**, 12588 (2014).
51. Y. Zeng, R. Hao, B. Xing, Y. Hou, and Z. Xu, *Chem. Commun.*, **46**, 3920 (2010).
52. C. Liang, T. Zhai, W. Wang, J. Chen, W. Zhao, X. Lu, and Y. Tong, *J. Mater. Chem. A*, **2**, 7214 (2014).